

Transition-metal dichalcogenide heterostructure solar cells: A numerical study

A. Thilagam*

Information Technology, Engineering and Environment,
University of South Australia, Australia 5095.

We evaluate the tunneling short-circuit current density J_{TU} in a $p-i-n$ solar cell in which the transition metal dichalcogenide heterostructure (MoS_2/WS_2 superlattice) is embedded in the intrinsic i region. The effects of varying well and barrier widths, Fermi energy levels and number of quantum wells in the i region on J_{TU} are examined. A similar analysis is performed for the thermionic current J_{TH} that arises due to the escape and recapture of charge carriers between adjacent potential wells in the i -region. The interplay between J_{TU} and J_{TH} in the temperature range (300 K - 330 K) is examined. The thermionic current is seen to exceed the tunneling current considerably at temperatures beyond 310 K, a desirable attribute in heterostructure solar cells. This work demonstrates the versatility of monolayer transition metal dichalcogenides when utilized as fabrication materials for van der Waals heterostructure solar cells.

I. INTRODUCTION

Low dimensional transition metal dichalcogenides (TMDCs) with the formula MX_2 ($\text{M} = \text{Mo}, \text{W}, \text{Nb}$ and $\text{X} = \text{S}, \text{Se}$) are currently studied with great interest due to their potential applications in optoelectronics [1–4] and photonics [5–9]. TMDCs possess intra-layer metal planes that are held between the atomic planes of a group VI element by covalent bonding, while the inter-layers are weakly positioned by van der Waals forces. Mechanical exfoliation using scotch tape techniques [10] and more recent exfoliation techniques [11–13] allow convenient fabrication of quality monolayers that display a range of band-gaps within the visible spectrum. Monolayers of well known TMDCs (MoS_2 , MoSe_2 , WS_2 and WSe_2) possess direct band-gaps [14] unlike their bulk counterparts that display indirect band-gaps. Due to the confinement of charge carriers, low dimensional transition metal dichalcogenides possess unique photoluminescence properties that differ vastly from those in the bulk systems. The widely studied molybdenum disulphide (MoS_2) has an indirect bandgap of 1.29 eV in bulk and is optically active in the visible range with direct bandgap of 1.8 eV in the monolayer form. The conduction band maximum and valence band minimum (VBM) are located at the K symmetry points of the direct bandgap [14, 15]. The photoluminescence is enhanced even at room temperatures with occurrence of notable spin-orbit splittings (0.15 – 0.46 eV) due to a lack of inversion symmetry at the valence bands [16].

Transition metal dichalcogenide heterostructures are designed by stacking at least two different monolayers (MoS_2/WS_2 , $\text{MoS}_2/\text{MoSe}_2$ or $\text{WS}_2/\text{MoSe}_2$) in alternating series. These systems possess direct band gaps that range approximately from 0.8 eV to 1.7 eV [17–21]. The low dimensional TMDCs are based on the van der Waals interaction at atomically even interfaces where dangling bonds are noticeably absent. Consequently, lattice matching complications do not arise giving rise to a wide choice in two-dimensional layer materials that can be used to fabricate van der Waals heterostructures. Solar cells based on silicon on the other hand experience light-induced degradation and are limited by the indirect bandgap of 1.1 eV so that light absorption is restricted to the visible and near-infrared range [22–24]. Monolayer TMDCs with thickness of less than 10 Å absorb up to 5 to 10% incident sunlight, one order of magnitude higher than in GaAs and Si materials [25]. The optimized graphene/ MoS_2/n -Si solar cell system possess a conversion efficiency of 11.1% [26] which is remarkably high for a photovoltaic device derived from MoS_2 thin films. A solar cell configuration based on vertically stacked Au/ MoS_2 /ITO PV devices yields a high short-circuit photocurrent density of 20.9 mA/cm² and power-conversion efficiencies of up to 2.8% under AM1.5G illumination [27]. The bandgap engineering possibilities of monolayer TMDCs are thus desired for photovoltaic applications [25, 27, 28].

In the WSe_2/WS_2 p-n heterojunction, a type-II band alignment [29] results from the efficient separation of electrons and holes which is desirable for enhanced photovoltaic effects. Similar physical separations of electrons and holes have also been observed in the type-II bilayers of alternative selenides and sulfides ($\text{WS}_2/\text{MoSe}_2$ and $\text{MoS}_2/\text{WSe}_2$) [17]. Measurements from a combined photoluminescence spectroscopy and optical pump-probe spectroscopy show direct evidence of charge transfer in photo-excited MoS_2/WS_2 heterostructures [30]. The time of transfer of holes in the MoS_2 layer to the WS_2 layer is estimated to be less than 50 fs. First-principles density functional calculations confirm the occurrence of a type II MoS_2/WS_2 heterostructure [31] where the electron and hole states at the optically active K point are localized in different monolayers. The rapid rate of charge separation [30] is evidence that the high exciton binding energies [14, 32–36] does not present as an obstacle to the transfer of charge carriers in MoS_2/WS_2 heterostructures. The newly formed excitons appear to be ionized rapidly into free electron-hole pairs due

*thilaphys@gmail.com

to a built-in electric field that is created when carrier states are aligned differently in the monolayers. The exact strength of the internal field may be determined using computational techniques that probe the hybridized electronic states at the heterojunction interfaces and including details of interactions of photo-excited states with lattice vibrational modes.

The ultrafast charge separation in heterostructures [17, 29–31] appears to be a key factor that can be exploited to fabricate solar cells with high conversion efficiencies. This work examines whether solar cells that incorporate heterostructures will give rise to enhanced photovoltaic features. The modification of the i region to include a quantum well of a narrow bandgap semiconductor between two wide bandgap barrier semiconductors was first proposed by Barnham and Duggan [37] so as to increase the photocurrent and to enhance the short-circuit current in solar cells. A notable increase in the short circuit current and solar conversion efficiency was seen in the case of GaAs/Al_xGa_{1-x}As heterostructure solar cells [38].

The superlattice solar cell is an extension of the single quantum well solar cell in which the high bandgap and low bandgap configuration of thin layers is repeated several times to enhance the tunneling of photo-generated carriers. The de-localization of charge carriers in distinct quantum wells depends on the strength of coupling between the potential wells. In strongly coupled systems, the superlattice structures form minibands which result in highly conductive systems with reduced recombination effects. A study on the GaAs/Al_xGa_{1-x}As superlattice solar cell [39], showed a large output power under intense illumination compared to the single quantum well solar cell. The efficiencies of solar cells based on the GaAs/Al_xGa_{1-x}As quantum well structure are optimized at critical well widths [40]. Similar studies have not been performed on transition metal dichalcogenides, hence in this work we examine a theoretical model in which the intrinsic i region is made up of the MoS₂/WS₂ superlattice within the $p-i-n$ solar cell system. Using numerical techniques we investigate whether the photocurrent is enhanced due to an increase in the number of multi-layer TMDCs with direct band gaps in the i region. This study aims to provide theoretical support to the experimental realization of novel solar cells based on transition metal dichalcogenides which enable enhanced photovoltaic attributes. The MoS₂/WS₂ system is chosen for this study as experimental and theoretical data [30, 31, 41] of the type-II band structure are easily available for these materials. While a specific material combination is considered here, the approach used in this work can be applied to other monolayer transition metal dichalcogenides [19–21, 41] as well.

The paper is organized as follows. In Sec. II we describe the basic operating principle of the $p-i-n$ solar cell with the MoS₂/WS₂ superlattice inserted in the i region. The general theory of the tunneling currents in the solar cell is discussed, and a relation for the tunneling current is used to examine the effects of varying well and barrier widths, Fermi energy levels and temperature in the i region. Comparison of the current estimates for a range of solar cell configurations are made with existing experimental results as well. In Sec.4, we examine the thermionic currents in the MoS₂/WS₂ superlattice $p-i-n$ solar cell and demonstrate the interplay between tunneling and thermionic currents in the temperature range (300 K - 330 K). We show that the thermionic current far exceeds the tunneling current at temperatures beyond 310 K which can be attributed to specific processes which are highly sensitive to the temperature. A brief discussion of the mechanisms that degrade the solar cell efficiency (trapping by surface defects, exciton recombination) is provided in Sec. III A and conclusions are finally summarized in Sec.IV.

II. NUMERICAL ANALYSIS OF THE BASIC $p-i-n$ SOLAR CELL

A. Basic model of the $p-i-n$ solar cell incorporating van der Waals heterostructures

A simple layout of the solar cell incorporating the vertically stacked MoS₂/WS₂ superlattice with a number of repeated distances is shown in Fig.1. It consists of a $p-i-n$ structure with alternating layers of TDMCs (MoS₂ and WS₂) within the i region. Each layer of MS₂ (M = Mo or W) is made up of a plane of Molybdenum or Tungsten atoms sandwiched between two planes of sulfur atoms. The hybrid layers are held by weak Van der Waals forces. The spatial separation of electrons and holes gives rise to the type-II band alignment of MoS₂/WS₂ heterostructure [31]. The valence band maximum lies in the WS₂ layer while the conduction band minimum lies in the MoS₂ layer. Accordingly the MoS₂/WS₂ bilayer heterojunction has an energy gap that is less than the band gaps of each of the two distinct monolayers. The monolayer MoS₂ presents as the barrier material for holes while monolayer WS₂ acts as the barrier material for electrons.

The conduction and valence band energy estimates for the MoS₂/WS₂ heterostructure as indicated in Fig.1 are based on first principle calculations [41] of the many-body Schrödinger equation derived using density functional theory (DFT) and the Hartree-Fock (HF) approximations. Likewise the height of the electron and hole potential wells indicated in Fig.1 are evaluated using estimates derived by Kang et. al. [41]. These values are based on the Heyd-Scuseria-Ernzerhof (HSE06) hybrid functional which combines Hartree-Fock and density functional approaches. We specifically utilize the HSE06 derived energy results [41] as these generally agree with experimental results [30] which show that the monolayer MoS₂ and WS₂ possess bandgaps of 2.39 eV and 2.31 eV respectively. The valence band maximum in MoS₂ is 350 meV less than the valence band maximum in WS₂. Both n -type [14, 15] and p -type [42] conductivities occur in the monolayer MoS₂ depending on the material (e.g SiO₂ or Nb) on which it is deposited. Here we assume that the p -region and n -region of the $p-i-n$ solar cell are derived using MoS₂, without too much focus on the details of the impurities in the n -type and p -type material as the specific details of the end regions of the solar cell do not affect the overall outcome of this study.

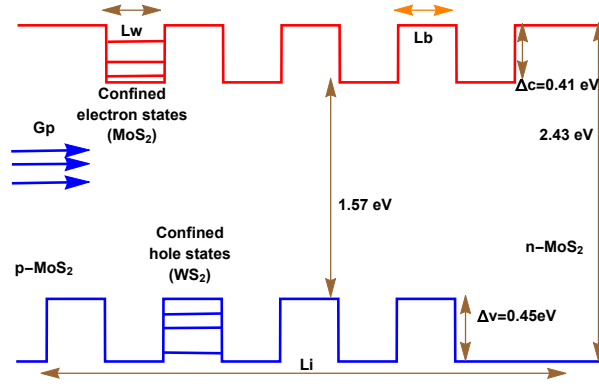


FIG. 1: Schematic structure of the p - i - n solar cell incorporating the type-II MoS₂/WS₂ superlattice. The bandgap differences (1.57 eV, 2.43 eV) are based on first principle calculations of the conduction and valence band energy estimates derived by Kang et. al. [41]. The depths of the potential well are quantified by Δ_c and Δ_v . G_p is the incoming photon flux, with arrows on the left denoting the incoming photons. The width of the intrinsic region is denoted by L_i .

The heterostructure in the i region is modeled as an alternating series of MoS₂/WS₂ with adjustable widths considered for the well and barrier material in the range, $L_w = L_b = 10$ to 14 \AA . These widths are justified on the basis of the Mo-W distance of $d = 13 \text{ \AA}$ over the vacuum region [18] and the monolayer MoS₂ height, $h = 9 \text{ \AA}$ [43]. The charge carriers occupy discrete energy levels within the well regions where the energy gap is lower than that of the barrier region due to quantum confinement effects. The whole system is subjected to an electric field in the operating regime.

B. Tunneling currents in the MoS₂/WS₂ heterostructure p - i - n solar cell

The presence of charge carriers outside the potential wells occurs with non-zero probabilities that are based on quantum mechanical rules. The tunneling process is classically forbidden for charge carriers which do not possess the extra energy required to escape the potential barriers. Following the solar cell model of Aperathitis et. al. [39], we consider that the confined charge carriers give rise to a tunneling current (J_{TU}) in the growth direction of the device alongside a thermionic current (J_{TH}) that occurs due to the escape of charge carriers from the quantum wells. The general current-density relationship for current densities is given by $J = nqv$ where q is the electron charge, n is the concentration of carriers with sufficient energy to overcome the potential barriers and $v(E)$ is the velocity of the carriers. The potential wells shown in Fig1 act as electron or hole reservoirs and influence the net electron propagation from the p-region to the n-region and hole propagation from the n-region to the p-region. The current flow is determined by the charge carrier tunneling probability $P(E)$, density of states $g(E)$, Fermi-Dirac occupation probability $f(E)$ and the photo-generation rate, $G_{ph} \alpha(\lambda) \exp(-\alpha(\lambda)x)$ where $\alpha(\lambda)$ is the absorption coefficient of the well material. In this work we consider that both the electron and hole contribute to the tunneling short-circuit current density due to the almost equivalent effective masses of electrons and holes in MoS₂, and similar rates of transfer of holes and electrons between the MoS₂ and WS₂ layers.

The tunneling short-circuit current density due to the charge carriers is expressed as

$$J_{TU}^i = q \left(\frac{A\tau}{L_i} \right) \int_0^{L_i} G_p \alpha(x) \exp[-\alpha(\lambda)x] dx \int_{E_i}^{E_f} g(E) v(E) P(E) \frac{1}{1 + e^{\frac{E-E_F}{kT}}} dE, \quad (1)$$

where $i = e, h$ denotes current due to electron or holes, E is the confinement energy of the carrier in the potential well, τ is the charge carrier transit time, A is the area of cross-section of the solar cell, L_i is the length of the intrinsic region. The Fermi-Dirac distribution function described by $1/[1 + \exp(\frac{E-E_F}{k_b T})]$ incorporates the temperature T and the quasi-Fermi levels $E_F = E_{Fe} (E_{Fh})$ which influences the propagation of electrons (holes). The Fermi level E_{Fe} lies within the MoS₂ band gap and is pinned below the bottom of the conduction bands. The Fermi level E_{Fe} for the n-type MoS₂ is recorded as -0.34 eV [44] which is marginally larger in magnitude than the Fermi level for WS₂ at -0.33 eV . To simplify the model calculations, we assume a common Fermi level for the MoS₂ and WS₂ layers. The estimates of the Fermi level E_{Fh} for the p-type MoS₂ [45] is not available in the literature. However the Fermi level range (0.32 to 0.37 eV) is justified as one can employ mechanical bending processes to control the Fermi-level shifts in two-dimensional materials [46] due to the localization of charges near the valence bands in MoS₂. The influence of the Fermi level on the tunneling short-circuit current density can thus be assessed by varying the Fermi levels E_{Fe} and/or E_{Fh} to lie in the range $0.32 \text{ eV} - 0.37 \text{ eV}$.

In Eq.1, we use the carrier lifetime $t_c = 100$ ps in MoS₂ [47] to estimate the carrier transit time, $\tau = t_c/g = 1$ ps at gain $g \approx 100$. The energy independent 2D density of states is given by $g(E) = \frac{g_s g_v m_i}{2\pi\hbar^2}$ where $g_s=2$ and $g_v=2$ are the respective spin and valley degeneracy factors, and \hbar and m_i are the reduced Planck constant and effective mass of the electron (m_e) or hole (m_h). To simplify the numerical analysis, we assume the effective mass to be an invariant of position in the heterostructure system. The absorption coefficient for the MoS₂ depends on the incident wavelength, and in this work we employ the empirical estimate of $\alpha(\lambda) = 3 \times 10^5 \text{ cm}^{-1}$ at the absorption wavelength of 530 nm [48]. The velocity of the electrons can be determined by employing $v(E) = \sqrt{2(\Delta_c - E)/m}$ where Δ_c is the conduction band discontinuity (shown in Fig 1). A similar relation can be used to determine the velocity of the holes using Δ_v , the valence band discontinuity. For energies less than the barrier height, $E < \Delta_c$, the tunneling probability function $P(E)$ associated with electrons (cf. Eq.1) is computed using

$$P(E) = \left(1 + \frac{\Delta_c^2 \sinh^2(k_b L_b)}{4E(\Delta_c - E)}\right)^{-1} \quad (2)$$

where the potential barrier factor $k_b = (\sqrt{2m_e(\Delta_c - E)}/\hbar)$. The expression for $P(E)$ associated with holes can likewise be derived using Δ_v . The tunneling probability function $P(E)$ in Eq.2 varies from the one employed by Aperathitis et. al. [39]

$$P_2(E) = \frac{16E(\Delta_c - E)}{\Delta_c^2} \exp(-k'_b \sqrt{1 - E/\Delta_c}) \quad (3)$$

where the potential barrier factor $k'_b = 2L_b(\sqrt{2m_e\Delta_c}/\hbar)$. In this study, we evaluate the current density using the two different forms of the tunneling probability functions (Eq.2, 3) to make comparison of the two functions using the computed values of J_{TU} .

The minimum (maximum) allowed energy in the quantum wells, E_i (E_f) in Eq.1 can be determined using the transcendental equations

$$\begin{aligned} \tan(\eta) &= \sqrt{\left(\frac{\sigma_0}{\eta}\right)^2 - 1} \quad (\text{even parity}), \quad -\cot(\eta) = \sqrt{\left(\frac{\sigma_0}{\eta}\right)^2 - 1} \quad (\text{odd parity}) \\ \eta &= \frac{L_w}{2} \sqrt{\frac{2m_e}{\hbar^2} E}, \quad \sigma_0 = \frac{L_w}{2} \sqrt{\frac{2m_e}{\hbar^2} \Delta_c} \end{aligned} \quad (4)$$

The energies E_i and E_f are quantified relative to the quasi-Fermi levels, E_{Fe} or E_{Fh} which lie in the vicinity of the MoS₂ conduction or valence bands, respectively. Substitution of $P(E)$ in Eq.2 into Eq.1 will yield a simpler form of the tunneling current due to electron propagation

$$\begin{aligned} J_{TU}^e &= \frac{8\sqrt{2}A q \tau g_s g_v \sqrt{m_e} \Delta_c}{\pi\hbar^2 L_i} G_p [1 - \exp(-\alpha L_i)] \int_{E_i}^{E_f} (1 - E/\Delta_c)^{1/2} \\ &\quad \times \left(1 + \frac{\Delta_c^2 \sinh^2(k_b L_b)}{4E(\Delta_c - E)}\right)^{-1} \frac{1}{1 + e^{\frac{E - E_F}{kT}}} dE. \end{aligned} \quad (5)$$

A relation similar to Eq.5 is applicable for the tunneling current due to hole propagation, J_{TU}^h . The integral over the carrier energies in Eq.5 is evaluated using the minimum and maximum allowed energies E_i and E_f (cf. Eq.4) based on given values of A , G_p and width of the intrinsic region, L_i . In the 400-700 nm range of the visible region of the AM1.5G solar spectrum, the average incident photon flux is evaluated to be $G_p = 1 \times 10^{17} \text{ cm}^{-2} \text{ s}^{-1}$. The effect of the number of wells n in the intrinsic region is examined by setting $L_i = n(L_w + L_b)$. The junction area A obviously determines the magnitude of the current density J_{TU} . In a study involving the GaAs/Al_xGa_{1-x}As superlattice solar cell system [39], a small junction area $A = 4 \times 10^{-3} \text{ cm}^2$ gave rise to a tunneling short-circuit current density J_{TU} in the range 3.5 to 43 mA/cm². This result also depended on device parameters (L_w , L_b) in the i -region and temperature. In a recent work by Tsai et. al. [49], a Al-contacted monolayer MoS₂/p-Si solar cell of area 1 cm × 1 cm was fabricated with doping concentration between 3.2×10^{16} and $2.5 \times 10^{17} \text{ cm}^{-3}$. This system displayed the open circuit voltage V_{oc} of 0.38 to 0.41 V and a short-circuit current J_{sc} from 21.66 to 22.36 mA/cm² with an efficiency of 5.23%. One needs to exercise caution when comparing results as solar cells of different configurations and dimensions are used in various studies. In this work a small value of $A = 1 \times 10^{-4} \text{ cm}^2$ is chosen as we expect a short-circuit current that is comparable to experimental observations [49] due to incorporation of the MoS₂/WS₂ superlattice in the solar cell system.

The results in Table-I obtained using the specified parameters for the i -region illustrate the importance of incorporating quantum wells within the p - i - n solar cell. At a constant width L_i of the intrinsic region, the total current density J_{TU} increases with well period before a decrease occurs beyond an optimum well period (about 36) with $L_w = L_b = 14 \text{ \AA}$. There are competing factors which account for the peak in current density observed at the optimum well period shown in Fig.2 for the parameters

TABLE I: Parameters used to model the i -region of the p - i - n solar cell. The total current density $J_{TU} = J_{TU}^e + J_{TU}^h$ is evaluated using Eq.5, at temperature $T = 300$ K and is based on the tunneling probability function given in Eq.2. J_{TU} is given in units of mA/cm². The electron and hole energies (E_i^e , E_i^h) are calculated relative to the bottom of the quantum well. The total width of intrinsic region is fixed at $L_i \approx 0.1 \mu$ m. The magnitude of the Fermi energy levels E_{Fe} and E_{Fh} are taken to be 0.34 eV. The effective mass of the electron $m_e = 0.51 m_o$ (MoS₂) and hole $m_h = 0.42 m_o$ (WS₂) given in terms of the free-electron mass m_o are retrieved from Ref.[50]. The junction area, $A = 1 \times 10^{-4}$ cm² while the carrier transit time, $\tau = 1$ ps. Based on the AM1.5G solar spectrum, the average incident photon flux is evaluated to be $G_p = 1 \times 10^{17}$ cm⁻² s⁻¹. The current density estimates included within the brackets below are evaluated using the tunneling probability function given in Eq.3.

Well period	L_w (Å)	L_b (Å)	E_i^e (eV)	E_i^h (eV)	J_{TU}^e (mA/cm ²)	J_{TU}^h (mA/cm ²)	J_{TU} (mA/cm ²)
56	9	9	0.21	0.25	12.42 (13.98)	4.08 (4.68)	16.50 (18.66)
50	10	10	0.20	0.22	18.49 (20.02)	6.77 (7.46)	25.26 (27.48)
45	11	11	0.18	0.21	24.36 (25.66)	9.92 (10.59)	34.28 (36.25)
42	12	12	0.16	0.19	28.30 (29.21)	12.71 (13.26)	41.01 (42.47)
38	13	13	0.15	0.17	31.03 (31.68)	15.29 (15.72)	46.32 (47.40)
36	14	14	0.14	0.16	30.64 (31.04)	16.48 (16.78)	47.12 (47.82)
30	16.5	16.5	0.11	0.13	24.63 (24.74)	16.00 (16.09)	40.63 (40.83)
25	20	20	0.09	0.10	11.84 (11.85)	9.52 (9.53)	21.32 (21.38)

specified in Table-I. An increase in the number of potential wells in i -region enhances the current density. On the other hand, a larger number of wells correspond to decreased well width for which the minimum energy levels of the confined charge carriers are increased. This in turn lowers the tunneling probability through the i -region of the p - i - n solar cell restricting further rise in J_{TU} . We note that the total current density J_{TU} evaluated using Eq.5 in Table-I is of the same order in magnitude as the experimental short-circuit current density of 33.4 mA/cm² [26] derived from the trilayer-graphene/MoS₂/n-Si solar cell with a 9 nm MoS₂ film. This optimized solar cell configuration resulted in the photovoltaic efficiency of 11.1% [26]. Although direct comparison of results is challenging due to differences in solar cell configurations, our results nevertheless demonstrate the potential for the MoS₂/WS₂ superlattice p - i - n solar cell to produce equivalent or larger photovoltaic efficiencies under favorable operating conditions.

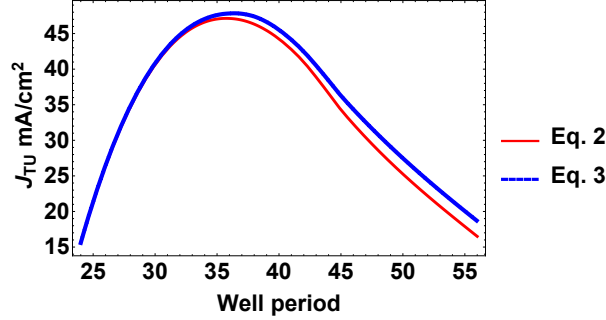


FIG. 2: The total current density $J_{TU} = J_{TU}^e + J_{TU}^h$ (mA/cm²) as function of the well period at temperature 300 K and Fermi energy levels $E_{Fe} = E_{Fh} = 0.34$ eV. All other parameters, including the variables L_w and L_b , are the same as those used to obtain the results in Table-I. The estimates are computed using Eq.5, the tunneling probability function $P(E)$ (Eq.2, red solid) and $P_2(E)$ (Eq.3, blue solid).

The effect of the Fermi energy levels E_{Fe} and E_{Fh} on the total current density $J_{TU} = J_{TU}^e + J_{TU}^h$ evaluated using the tunneling probability function $P(E)$ (Eq.2) is shown in Fig. 3a. The well period = 45, $L_w = 11$ Å, $L_b = 11$ Å and other parameters are the same as those used to generate the results of Table-I. A significant increase in J_{TU} occurs when the Fermi levels are positioned closer to the conduction or valence bands. At the higher temperature of 300 K, J_{TU} is enhanced by a factor of 7 when the Fermi levels are shifted closer to the conduction/valence bands by 0.32 eV from 0.38 eV. These results may be linked to the lower “activation energies” that is needed for the confined charge carriers to tunnel through the potential barriers.

The wave-function of the charge carrier with larger mass experiences faster decay in the barrier material compared to the carrier with a lighter mass. The energy estimates in Table-I show that the minimum energy levels of the electron with higher mass ($0.51 m_o$) is lower than the energy levels of the hole ($0.42 m_o$). The minimal energy level appear to be a dominating factor, as it influences the tunneling probability through the i -region, accordingly the current density J_{TU} due to electrons is higher than that due to holes for the parameters listed in Table-I. The transmission probability of a trapped charge carrier also decreases with

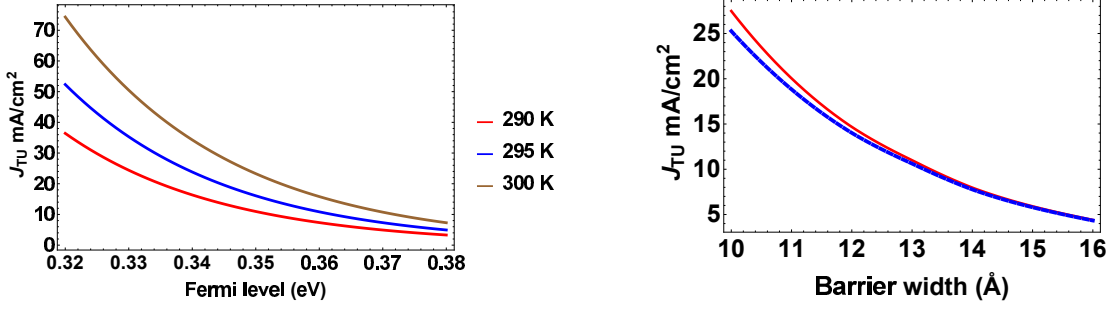


FIG. 3: (a) The total current density $J_{TU} = J_{TU}^e + J_{TU}^h$ (mA/cm²) as function of the Fermi levels $E_{Fe} = E_{Fh}$ at temperatures (290 K, 295 K, 300 K) computed using Eq.5 and an analogous relation for holes. The well period = 45 and $L_w = 11$ Å, $L_b = 11$ Å. All other parameters (except for the Fermi energy levels) are given in Table-I.

(b) The total current density J_{TU} computed using the tunneling probability function $P(E)$ (Eq.2, lower blue curve) and $P_2(E)$ (Eq.3, upper red curve). The well width is fixed at $L_w = 10$ Å and the barrier width L_b is varied such that the total width of intrinsic region remains constant at $L_i = n(L_w + L_b) \approx 0.1$ μm. All other parameters are the same as those used to generate the results of Table-I.

the thickness of the barrier as shown in Fig. 3b where the total current density J_{TU} is computed using the tunneling probability function $P(E)$ (Eq.2) and $P_2(E)$ (Eq.3) for comparison purposes. The well width is fixed at $L_w = 10$ Å and the barrier width L_b is varied such that the total width of intrinsic region remains constant at $L_i = n(L_w + L_b) \approx 0.1$ μm. The other parameters used to obtain the results in Fig. 3b are given in Table-I. A slightly elevated J_{TU} is obtained with the tunneling probability function $P_2(E)$ (Eq.3) at barrier widths ≈ 10 Å, otherwise the two probability distributions yield almost similar estimates of the current density. The results in Fig. 3 show that J_{TU} is enhanced in a solar cell with decreased barrier widths and at elevated temperatures, the latter two factors contributing to the increased energies of charge carriers which enhances the tunneling effects.

III. THERMIONIC CURRENTS IN THE MoS₂/WS₂ SUPERLATTICE *p-i-n* SOLAR CELL

A thermionic current [51–57] is induced when charge carriers escape from one quantum well and are recaptured by the adjacent well without undergoing recombination processes in the *i*-region. The thermionic emission is an important mechanism that induces current across the interface layers of the MoS₂/WS₂ system. It is evaluated based on the positions of the conduction and valence bands and changes in effective masses of the charge carriers that transverse quantum mechanically through the series of potential barriers. In order to obtain estimates of the thermionic current for the MoS₂/WS₂ superlattice *p-i-n* solar cell, we consider the thermionic theory of Wu et. al. [51] for bulk systems as well as its adaptation to two-dimensional systems [51–53]. We employ the thermionic current of the form

$$J_{TH} = \frac{\sigma}{L_q} A_r T^\alpha \sqrt{\frac{m_{e1}m_{e2}}{m_{e1} + m_{e2}}} \exp\left(-\frac{E_b - E_{Fe}}{k_B T}\right) \quad (6)$$

where $A_r = \frac{\sqrt{2\pi}ek_B^\alpha}{\hbar^2}$ is the Richardson constant [58] at $\alpha = 3/2$, $L_q = L_b + L_w$ is the quantization length and σ is a material dependent correction factor which is ≈ 0.5 for a wide range of material systems. The factor $\alpha = 2$ for bulk materials and is $\frac{3}{2}$ for two-dimensional systems [52, 53] and E_{Fe} is the Fermi energy level that lies in the vicinity of the conduction bands, and m_{e1} and m_{e2} are the respective electron masses in the MoS₂ and WS₂ monolayer regions. We set effective potential barrier energy $E_b = \Delta_c - E_1$ where Δ_c is the conduction band discontinuity (see Fig 1) and E_1 is the minimum energy in the quantum wells. We employ the values of E_i evaluated for the specific cell configuration as detailed in Table-I. The minimum energy E_1 was not included in the computation of the thermionic current in earlier works [51–53, 59]. The inclusion of this minimum energy adds greater accuracy to the evaluation of the effective barrier via $E_b = \Delta_c - E_1$. The thermionic current due to holes appears in the same form as Eq.6, with substitution of the valence band discontinuity Δ_v and m_{h1} and m_{h2} , the respective hole masses in the WS₂ and MoS₂ monolayers.

A standard form for the thermionic current (Eq.6) is lacking in the literature, partly due to inconsistencies in the definition employed for the Richardson constant, A_r [52, 53]. Moreover the correction factor σ in Eq.6 has not been considered in earlier works. A reflection factor which takes into account backscattering processes and interactions with secondary electrons [60] is expected to contribute to a more realistic modeling of the thermionic current. In order to obtain quantitative estimates of the thermionic current J_{TH} using Eq.6, we employ $\sigma = 0.5$ and consider the masses of the charge carriers in the MoS₂ and WS₂ monolayers as $m_{e1} = 0.51$, $m_{e2} = 0.31$, $m_{h1} = 0.42$, $m_{h2} = 0.58$ [50]. In Fig. 4a we plot the thermionic current J_{TH} as a function of the temperature based on the minimum energies E_1 for electrons and holes (Table-I) and the common Fermi energy

levels $E_{F_e} = E_{F_h} = 0.34$ eV. The results indicate that the thermionic current is dominant in systems with small potential well widths, rising rapidly with temperature for all system configurations.

As different formalisms are used to estimate the tunneling and thermionic currents in this study, we use the ratios $J^r_{TH} = \frac{J_{TH}(T)}{J_{TH}(280K)}$ and $J^r_{TU} = \frac{J_{TU}(T)}{J_{TU}(280K)}$ to compare the rise of the different current components with temperature. Fig. 4b demonstrates the interplay between tunneling and thermionic currents in the temperature range (300 K - 330 K). While the difference between the currents is not significant in the temperature range (270 K - 290 K), the thermionic current far exceeds the tunneling current at temperatures beyond 310 K. This can be attributed to the higher probabilities of charge carriers with increased energies that escape from the potential well, which is also quantified by the exponential function in Eq.6. To this end, the thermionic current plays an important role in enhancing the performances of heterostructure solar cells at elevated temperatures.

The combined results in Figs. 2 and 4 show that the output currents in a heterostructure solar cell can be controlled to a desirable level by adjusting the dimensions of the potential well and barrier widths of the superlattice in the i region. The Fermi energy levels also have a strong influence on the total current density ($J_{TU} + J_{TH}$). The quantitative details of the influence of the depth of potential wells on the current densities have not been examined here. In general, deep wells (large Δ_c , Δ_v in Fig. 1) tend to hold a higher density of carriers than shallow wells, which contributes to increased current densities. Further investigation is needed to examine if deep wells impede the thermionic process as it is likely that the recapturing of emitted charge carriers becomes less efficient when the well depths Δ_c , Δ_v are made larger.

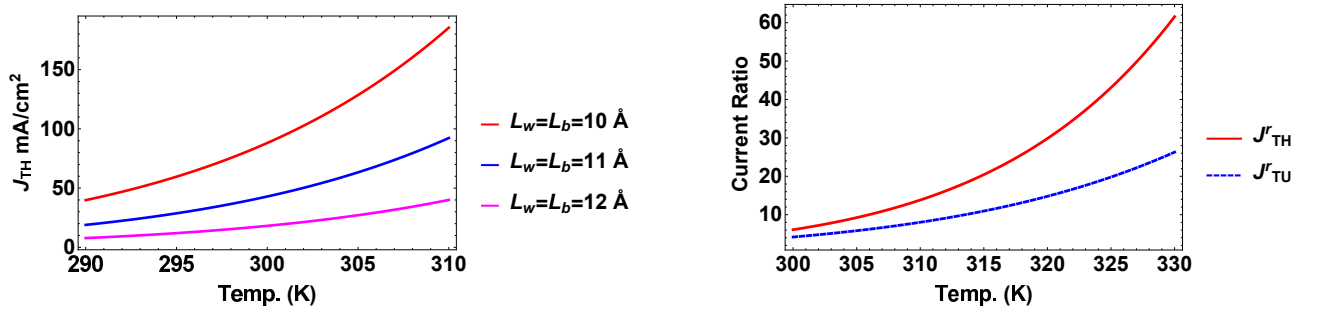


FIG. 4: (a) The thermionic current density J_{TH} (Eq.4) as function of the temperatures at three different well and barrier widths. We set $\sigma = 0.5$ with masses of the charge carriers in the MoS₂ and WS₂ monolayers taken as $m_{e1} = 0.51$, $m_{e2} = 0.31$, $m_{h1} = 0.42$, $m_{h2} = 0.58$ [50]. The minimum energies E_1 for electrons and holes are given in Table-I and the common Fermi energy levels $E_{F_e} = E_{F_h} = 0.34$ eV. (b) Comparison of the rise of the tunneling and thermionic currents with temperature based on the ratios, $J^r_{TH} = \frac{J_{TH}(T)}{J_{TH}(T_o)}$ and $J^r_{TU} = \frac{J_{TU}(T)}{J_{TU}(T_o)}$ where $T_o = 280$ K. The widths $L_b = L_w = 14$ Å, and $E_i^e = 0.14$ eV, $E_i^h = 0.16$ eV are used in Eqs. 5 and 6 to compute the current densities.

A. Factors that decrease the conversion efficiency in the p - i - n heterostructure solar cell

The conversion efficiency quantifies the fraction of solar energy that is transformed via photovoltaic action into electricity. It is dependent on several parameters [61–63] which have not been actively examined in this work. The appearance of a peak in current density J_{TU} (Fig. 2) however implies that the conversion efficiency is not a monotonic function of the number of potential wells in a heterostructure solar cell. The fast ionization of excitons enhances J_{TU} and contributes to increased efficiencies in heterostructure solar cells. However excitons undergo fast relaxation due to interactions with phonons [64] and may recombine radiatively instead of undergoing ionization into free carriers. The defect assisted scattering and trapping of excitons by surface states [65] may also act to decrease the efficiencies of layered transition metal dichalcogenides solar cells. The fast capture of excitons by mid-gap defects through Auger processes [66] and exciton-exciton annihilation [67, 68] are alternative processes that may result in decreased efficiencies of solar cells.

The formation of the negatively charged trion which is a three-body bound state of two electrons and one hole [69] is expected to interfere with photoconductive properties of the solar cell. The charged exciton in layered transition metal dichalcogenides are highly stable even at room temperatures [35, 70, 71]. The high effective mass of the trion give rise to lower mobilities with decreased probabilities of tunneling through the potential barriers in the i -region of the solar cell. To this end, the formation of charged exciton complexes is expected to reduce solar cell efficiencies. A detailed examination of the expected decrease in efficiency due to creation of trion quasi-particles in solar cells fabricated using transition-metal dichalcogenides is planned for future investigations.

IV. CONCLUSION

In summary, we have investigated the importance of embedding the MoS₂/WS₂ superlattice in the intrinsic *i* region of a *p-i-n* solar cell structure. A type-II band alignment of MoS₂ and WS₂ acts as the driving force for the effective charge separation and enabling enhanced performances for photovoltaic applications. Our results show that the tunneling short-circuit current density J_{TU} increases with the incorporation of quantum wells in the intrinsic *i* region. The tunneling current density is dependent on the potential well width, barrier width, Fermi energy levels and temperature. A decrease in the short-circuit current density occurs when the optimum number of quantum wells is exceeded in the *i* region when the overall width of the intrinsic region is held constant. The positioning of Fermi energy levels closer to the conduction or valence bands is seen to give rise to a marked increase in J_{TU} .

The effects of varying well and barrier widths and Fermi energy levels on the thermionic current J_{TH} show a trend similar to that displayed by the tunneling current. The interplay between J_{TU} and J_{TH} in the temperature range (300 K - 330 K) is analysed. The thermionic current is seen to far exceed the tunneling current at temperatures beyond 310 K. We emphasize the prominent role played by the thermionic current in enhancing the performances of heterostructure solar cells at elevated temperatures. Our results predict that the heterostructure solar cell is better suited to yield higher current densities compared to homogeneous *p-i-n* solar cells made of transition-metal dichalcogenides. It would be worthwhile to see if experimental studies can produce results which are consistent with our theoretical findings. In future investigations, the various loss mechanisms (exciton recombination, exciton-exciton annihilation) and polaronic effects [72–74] may need to be incorporated for a more realistic modeling of the heterostructure solar cells.

Lastly, the charge separation resulting in electron confinement to the MoS₂ layer and hole confinement to the WS₂ layer typifying the type-II band alignment at the MoS₂/WS₂ interface presents a unique functionality that can be exploited in heterostructure devices. The results of this study while focussed on the MoS₂/WS₂ system points to new directions for novel solar cell designs based on alternative combinations of MoSe₂, MoTe₂ and WSe₂. Innovative solar cell configurations that incorporate vertical or lateral heterostructures [17, 75] are expected to replace crystalline silicon solar cells which currently are limited by their maximum achievable solar conversion efficiencies.

-
- [1] M.-Y. Li, C.-H. Chen, Y. Shi, and L.-J. Li, *Materials Today* (2015).
 - [2] S.-L. Li, K. Tsukagoshi, E. Orgiu, and P. Samorì, *Chemical Society Reviews* **45**, 118 (2016).
 - [3] V. Perebeinos, *Nature nanotechnology* **10**, 485 (2015).
 - [4] S. Ghatak, A. N. Pal, and A. Ghosh, *Acs Nano* **5**, 7707 (2011).
 - [5] X. Gan *et al.*, *Applied physics letters* **103**, 181119 (2013).
 - [6] S. Wu *et al.*, *2D Materials* **1**, 011001 (2014).
 - [7] A.-P. Luo *et al.*, *Photon. Res* **3**, A69.
 - [8] D.-S. Tsai *et al.*, *Acs Nano* **7**, 3905 (2013).
 - [9] G. Eda and S. A. Maier, *Acs Nano* **7**, 5660 (2013).
 - [10] K. Novoselov *et al.*, *Proceedings of the National Academy of Sciences of the United States of America* **102**, 10451 (2005).
 - [11] X. Fan *et al.*, *Nano letters* **15**, 5956 (2015).
 - [12] E. Varrla *et al.*, *Chemistry of Materials* **27**, 1129 (2015).
 - [13] M. Chen *et al.*, *ACS nano* **9**, 8773 (2015).
 - [14] K. F. Mak, C. Lee, J. Hone, J. Shan, and T. F. Heinz, *Physical Review Letters* **105**, 136805 (2010).
 - [15] K. F. Mak *et al.*, *Nature materials* **12**, 207 (2013).
 - [16] Z. Zhu, Y. Cheng, and U. Schwingenschlögl, *Physical Review B* **84**, 153402 (2011).
 - [17] H. Terrones, F. López-Urías, and M. Terrones, *Scientific reports* **3**, 1549 (2013).
 - [18] H.-P. Komsa and A. V. Krasheninnikov, *Physical Review B* **88**, 085318 (2013).
 - [19] R. Ionescu *et al.*, *Chemical Communications* **51**, 11213 (2015).
 - [20] B. Amin, N. Singh, and U. Schwingenschlögl, *Physical Review B* **92**, 075439 (2015).
 - [21] G. S. Duesberg, *Nature materials* **13**, 1075 (2014).
 - [22] D. E. Carlson and C. R. Wronski, *Applied Physics Letters* **28**, 671 (1976).
 - [23] F. Demichelis, A. Tagliaferro, and E. Tresso, *solar Cells* **14**, 149 (1985).
 - [24] A. Thilagam and J. Singh, *Journal of non-crystalline solids* **288**, 66 (2001).
 - [25] M. Bernardi, M. Palummo, and J. C. Grossman, *Nano letters* **13**, 3664 (2013).
 - [26] Y. Tsuboi *et al.*, *arXiv preprint arXiv:1503.05380* (2015).
 - [27] S. Wi *et al.*, *ACS nano* **8**, 5270 (2014).
 - [28] S. L. Howell *et al.*, *Nano letters* **15**, 2278 (2015).
 - [29] N. Huo *et al.*, *Small* **11**, 5430 (2015).
 - [30] X. Hong *et al.*, *Nature nanotechnology* (2014).
 - [31] K. Kośmider and J. Fernández-Rossier, *Physical Review B* **87**, 075451 (2013).
 - [32] A. Ramasubramaniam, *Physical Review B* **86**, 115409 (2012).

- [33] T. Cheiwchanchamnangij and W. R. Lambrecht, *Physical Review B* **85**, 205302 (2012).
- [34] H.-P. Komsa and A. V. Krasheninnikov, *Physical Review B* **86**, 241201 (2012).
- [35] A. Thilagam, *Journal of Applied Physics* **116**, 053523 (2014).
- [36] H. M. Hill *et al.*, *Nano letters* **15**, 2992 (2015).
- [37] K. W. Barnham and G. Duggan, *Journal of Applied Physics* **67**, 3490 (1990).
- [38] K. Barnham *et al.*, *Applied physics letters* **59**, 135 (1991).
- [39] E. Aperathitis *et al.*, *Solar energy materials and solar cells* **70**, 49 (2001).
- [40] A. Thilagam, J. Singh, and P. Stulik, *Solar energy materials and solar cells* **50**, 243 (1998).
- [41] J. Kang, S. Tongay, J. Zhou, J. Li, and J. Wu, *Applied Physics Letters* **102**, 012111 (2013).
- [42] M. R. Laskar *et al.*, *Applied Physics Letters* **104**, 092104 (2014).
- [43] B. W. Baugher, H. O. Churchill, Y. Yang, and P. Jarillo-Herrero, *Nano letters* **13**, 4212 (2013).
- [44] L. Liu, S. B. Kumar, Y. Ouyang, and J. Guo, *Electron Devices, IEEE Transactions on* **58**, 3042 (2011).
- [45] K. Dolui, I. Rungger, and S. Sanvito, *Physical review B* **87**, 165402 (2013).
- [46] L. Yu, A. Ruzsinszky, and J. P. Perdew, *Nano letters* (2016).
- [47] R. Wang *et al.*, *Physical Review B* **86**, 045406 (2012).
- [48] A. Beal and H. Hughes, *Journal of Physics C: Solid State Physics* **12**, 881 (1979).
- [49] M.-L. Tsai *et al.*, *ACS nano* **8**, 8317 (2014).
- [50] Z. Jin, X. Li, J. T. Mullen, and K. W. Kim, *Phys. Rev. B* **90**, 045422 (2014).
- [51] C. Wu and E. Yang, *Solid-State Electronics* **22**, 241 (1979).
- [52] A. Anwar, B. Nabet, J. Culp, and F. Castro, *Journal of applied physics* **85**, 2663 (1999).
- [53] A. Allain, J. Kang, K. Banerjee, and A. Kis, *Nature Materials* **14**, 1195 (2015).
- [54] H. Shichijo, K. Hess, and B. Streetman, *Solid-State Electronics* **23**, 817 (1980).
- [55] S. Mottet and J. Viallet, Thermionic emission in heterojunctions, in *Proc. 3rd Int. Conf. on Simulation of Semiconductor Devices and Processes*, pp. 97–108, 1988.
- [56] A. Grinberg, *Physical Review B* **33**, 7256 (1986).
- [57] M. Grupen, K. Hess, and G. H. Song, Simulation of transport over heterojunctions, in *Proc. 4th Int. Conf. Simul. Semicon. Dev. Process* Vol. 4, pp. 303–311, 1991.
- [58] C. Crowell, *Solid-State Electronics* **8**, 395 (1965).
- [59] S. Hójfeldt and J. Mór, Selected Topics in Quantum Electronics, *IEEE Journal of* **8**, 1265 (2002).
- [60] A. Modinos, Secondary electron emission spectroscopy, in *Field, Thermionic, and Secondary Electron Emission Spectroscopy*, pp. 327–345, Springer, 1984.
- [61] P. Landsberg, H. Nussbaumer, and G. Willeke, *Journal of Applied Physics* **74**, 1451 (1993).
- [62] A. Nozik, *Physica E: Low-dimensional Systems and Nanostructures* **14**, 115 (2002).
- [63] M. Wolf, R. Brendel, J. Werner, and H. Queisser, *Journal of Applied Physics* **83**, 4213 (1998).
- [64] A. Thilagam, *Journal of Applied Physics* **119**, 164306 (2016).
- [65] H. Shi *et al.*, *ACS nano* **7**, 1072 (2013).
- [66] H. Wang *et al.*, *Physical Review B* **91**, 165411 (2015).
- [67] D. Sun *et al.*, *Nano letters* **14**, 5625 (2014).
- [68] S. Konabe and S. Okada, *Physical Review B* **90**, 155304 (2014).
- [69] A. Thilagam, *Physical Review B* **55**, 7804 (1997).
- [70] H. S. Lee, M. S. Kim, H. Kim, and Y. H. Lee, *Physical Review B* **93**, 140409 (2016).
- [71] T. C. Berkelbach, M. S. Hybertsen, and D. R. Reichman, *Physical Review B* **88**, 045318 (2013).
- [72] A. Thilagam, *Physica B: Condensed Matter* **464**, 44 (2015).
- [73] A. Matos-Abiague, *Journal of Physics: Condensed Matter* **14**, 4543 (2002).
- [74] A. Thilagam and A. Matos-Abiague, *Journal of Physics: Condensed Matter* **16**, 3981 (2004).
- [75] Y. Gong *et al.*, *Nature materials* **13**, 1135 (2014).